Preprint Title Multicomponent bionanocomposites based on clay-nanoarchitectures for electrochemical devices

Authors Giulia Lo Dico, Bernd Wicklein, Lorenzo Lisuzzo, Giuseppe Lazzara, Pilar Aranda and Eduardo Ruiz-Hitzky

Article Type Full Research Paper

Supporting Information File 1 Lo+Dico+et+al.+Supporting+info.docx; 906.4 KB

ORCID® iDs Giulia Lo Dico - https://orcid.org/0000-0001-9841-4399; Lorenzo Lisuzzo - https://orcid.org/0000-0001-6954-2754; Giuseppe Lazzara - https://orcid.org/0000-0003-1953-5817; Pilar Aranda - https://orcid.org/0000-0003-2196-0476; Eduardo Ruiz-Hitzky - https://orcid.org/0000-0003-4383-7698

Multicomponent bionanocomposites based on clay-nanoarchitectures for electrochemical devices

Giulia Lo Dico[1,2], Bernd Wicklein[1], Lorenzo Lisuzzo[2], Giuseppe Lazzara[2], Pilar Aranda[1], Eduardo Ruiz-Hitzky[1,*].

Address: [1]Instituto de Ciencia de Materiales de Madrid (ICMM), Consejo Superior de Investigaciones Científicas (CSIC), c/Sor Juana Inés de la Cruz 3, 28049 Madrid, Spain. [2]Dipartimento di Fisica e Chimica, Università degli Studi di Palermo, Viale delle Scienze pad 17, 90128 Palermo, Italy

Email: Eduardo Ruiz-Hitzky, eduardo@icmm.csic.es

* Corresponding author

Abstract

Based on the unique ability of defibrillated sepiolite (SEP) to form stable and homogeneous colloidal dispersions of diverse types of nanoparticles in aqueous media under ultrasonication, multicomponent conductive nanoarchitectured materials integrating halloysite nanotubes (HNT), graphene nanoplatelets (GNP) and chitosan (CHI) have been developed. The resulting nanohybrid suspensions could be easily conformed either as films or as foams, where each individual component plays a critical role in the biocomposite: HNT acts as nanocontainer for bioactive species, GNP provide electrical conductivity (enhanced by doping with MWCNT) and, the CHI polymer matrix introduces mechanical and membrane properties, which are of key significance for the development of electrochemical devices. The resulting characteristics open the way to use these active elements as integrated multicomponent materials for advanced electrochemical devices such as biosensors and enzymatic biofuel cells. This strategy can be regarded as an “a la carte menu”, where the selection of the nanocomponents provided with diverse properties will

determine a functional set of predetermined utility thanks to the SEP behavior to maintain stable colloidal dispersions of different nanoparticles and polymers in water.

Keywords

Halloysite nanotubes; sepiolite; carbon nanostructures; bionanocomposites;

electrochemical devices

Introduction

In recent years, the application of the “nanoarchitectonics concept” has contributed to develop a large variety of materials provided of new functionalities [1-5]. Under this umbrella, diverse type of functional materials based on clay minerals have been also prepared, being pillared-clays and polymer-clay nanocomposites the best known examples on this topic [6]. Besides classical layered silicates, clays showing other morphologies as it is the case of fibrous (sepiolite and palygorskite) and tubular (halloysite and imogolite) clays, could be also interesting nanoparticulated solids for application of such concept [7-10]. In this, context, sepiolite and palygorskite are attracting growing interest for being used in the development of nanoarchitectured materials of interest in applications dealing topics from catalysis to biomedicine [7]. The presence of silanol groups regularly disposed at the external surface of the clay fibers allow the easy assembly of diverse species facilitating the design and the building-up of numerous functional materials. On the other hand, tubular nanoclays, such as halloysite nanotubes (HNT), are interesting containers for controlled chemical reactions at nanoscale interfaces and delivery of active compounds thanks to their singular nature [11], which could be advantageous when integrated as component in nanoarchitectured materials.

Halloysite nanotubes are aluminosilicates of cylindrical shape with a length ranging between 500 and 1000 nm and a lumen diameter between 15-70 nm [12]. The lumen represents an ideal nanospace for the uptake and preservation of diverse functional species including drugs, proteins, and enzymes [13-17], even serving as nanoreactor for chemical processes within confined microenvironments [18]. Of particular interest is the use of HNT for the uptake of enzymes as it represents an excellent approach for the development of (bio)electro-chemical devices like biosensors and enzymatic

biofuel cells (EBC) [19-20]. However, one of the main problems limiting the preparation of HNT-based nanoarchitectured materials is the low colloidal stability of HNT in aqueous media that, for instance, ultimately leads to inhomogeneous and underperforming nanocomposites in spite of the different approaches that have been developed to obtain homogeneous dispersions within different polymeric matrices [21-22]. Therefore, other and more efficient colloidal stabilizers are needed to fully exploit the potential of HNT.

It has been recently observed that sepiolite fibrous clay mineral of rheological grade (see experimental section) develops highly stable and viscous suspensions by sonomechanical treatment in water. Disaggregated sepiolite dispersions are efficient suspension capacity enhancers for the stabilization of nanoparticles of different topologies and hydrophobic nature such as graphene nanoplatelets (GNP) and carbon nanotubes (MWCNT) in water [23-24]. In fact, following this approach it was possible to prepare multifunctional and homogeneous nanocomposite materials like self-supported sepiolite-nanocarbon hybrid buckypapers [23] and conducting bionanocomposites [24]. Therefore, the present study explores now the potential of sepiolite for stabilizing also aqueous HNT suspensions.

Sepiolite (SEP) is a microcrystalline hydrated magnesium silicate displaying a fibrous morphology with dimensions depending on the geological environment of is origin [25]. For instance, an aspect ratio of up to 100 and diameters ranging from 10 to 50 nm are usually observed in sepiolite samples from the Taxus Basin (Spain) deposits [26]. The singularity of this nanofibrous clay is its ability to largely disaggregate in water after ultrasound treatment, creating thus a rigid, percolated network that can sustain co-dispersed compounds or reinforce polymer matrices [23-24, 27]. Interestingly, HNT are known to maintain their ability to act as nanocontainer even when dispersed in a multicomponent system included in polymer matrices [20]. In this way, it has been observed that positively charged polymers such as chitosan (CHI) can electrostatically incorporate the previously loaded halloysite through interactions with its external surface, maintaining the lumen unaffected and therefore, offering interesting possibilities for further inclusion of diverse guest species [28-29]. In addition, the role of the polymer matrix is crucial to process advanced bionanocomposite materials either as films or as foams [30-32]. This type of hybrid materials offers the advantage of a large interface improving the contact efficiency between the entrapped active molecules and the external environment allowing the

development of promising devices for biosensing [33] and enzymatic biofuel cells (EBC) [34-35].

In this work, conducting multicomponent nanoarchitectured materials involving HNT, GNP, MWCNT, and CHI matrix were prepared and processed as films and foams from aqueous suspensions of the components dispersed under ultrasound irradiation as schematized in Fig. 1. The incorporation of glucose oxidase (GOx) into the HNT lumen has been chosen here as a showcase example for the immobilization of bioactive species, which can be crucial to design (bio)electro-chemical devices with high performance and long life-time. The SEP, GNP, and MWCNT components are also foreseen to behave as polymer nanofillers to ensure the mechanical strength and electrical conductivity of the prepared bionanocomposite films and foams. Moreover, MWCNT is to act as nanowires improving the contact between the active site of the immobilized enzymes and an electrode surface via direct electron transfer mechanism [36].

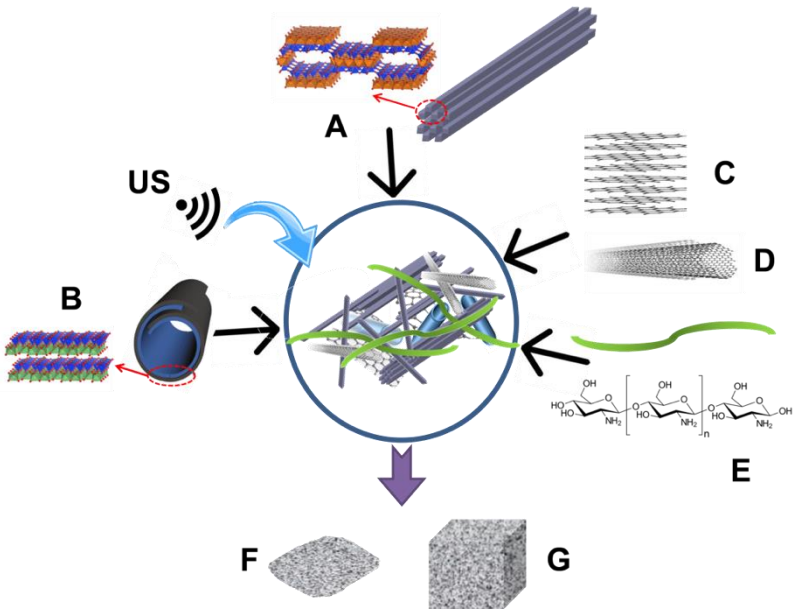

Figure 1. Schematic representation of the diverse components integrated in the bionanocomposite materials, comprising sepiolite fibrous clay (A), halloysite nanotubes (B), graphene nanoplatelets (C), multiwalled carbon nanotubes (D) and chitosan biopolymer (E), prepared in aqueous media under ultrasound irradiation (US). The resulting nanoarchitectured materials can be conformed as films (F) or foams (G).

The resulting multicomponent systems have advantages such as high electrical conductivity and flexibility that make the here reported bionanocomposite films appropriate components for biosensors [33] for glucose detection, while the relatively high porosity of the bioactive foams enhances the power density and operational stability of an enzymatic biofuel cells (EBC) [34].

Herein, the performance of the biosensor was evaluated by cyclic voltammetry exploiting the mediated electron transfer (MET) mechanism and the power density of the assembled biofuel cell is followed by polarization curves obtained with linear sweep voltammetry in the direct electron transfer (DET) mode.

Results and Discussion

Preparation of bionanocomposite films and foams

The preparation of multicomponent nanoarchitectured materials used as functional nanofiller in the further preparation of bioactive and conducting nanocomposites was carried out by mixing of SEP and HNT nanoclays with GNP and MWCNT in aqueous media assisted by sonomechanical treatment as schematized in Fig. 1. The generation of homogeneous and stable multicomponent dispersions in water (Fig. 2) can only be accomplished thanks to the rheological properties of the SEP fibrous clay (Pangel® S9) under ultrasound irradiation. Hence, the incorporation of these components within a polymeric (CHI) matrix results in composite materials, which are processed either as films or as foams. In agreement with previous works [23-24], the ultrasound treatment of this type of sepiolite in aqueous medium promotes the homogeneous dispersion of diverse nanoparticulated components present in that medium. It can be inferred that the disaggregated fibres of sepiolite form an interpenetrated network representing, in the present case, a steric hindrance for GNP, MWCNT, and HNT to re-bundle and hence, to avoid phase segregation and particle sedimentation.

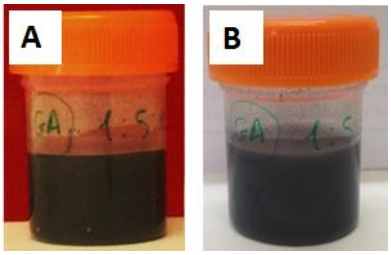

Figure 2. Photographs showing the macroscopic aspect of dispersions at 1 wt% of a multicomponent bionanocomposite (composition of Film-1 sample). A) as freshly prepared; B) after 5 months.

These dispersions remained stable for more than 5 months (Figure 2B) and proved to be suitable for preparing self-supported, flexible films by solvent casting (Figure 3B) as well as foams by freeze-casting (Figure 3C).

The lamellar arrangement of the bionanocomposite films is schematized in Figure 3A, while SEM images (Figure 3D,F) reveal that the components are uniformly distributed throughout the film and are organized as a compacted particle assembly within the chitosan matrix. Furthermore, the film cross-section (Figure 3F) displays the typical layered structure of solvent cast films from fibre dispersions [24, 27, 38]. Importantly, the access to the HNT lumen appears to remain unblocked despite their assembly with the other components (Figure 3H), which is crucial for the effective use of HNT as nanocontainer for bioactive molecules. The presence of MWCNT was not detected in the SEM images given their small size and low concentration (2-5 %) in the bionanocomposites.

Freeze-casting rendered foams of high mechanical consistency and shape-fidelity (Figure 3C). The foams display open, cell-like pores (Figure 3E,G) with a pore diameter of 13 ± 4 μm and a cell wall thickness of 0.2–0.4 μm (Figure S1), comparable to similar freeze-cast clay nanocomposite foams [39-40]. Halloysite nanotubes are visible on the surface of the cell wall with free access to the lumen (Figure 3I).

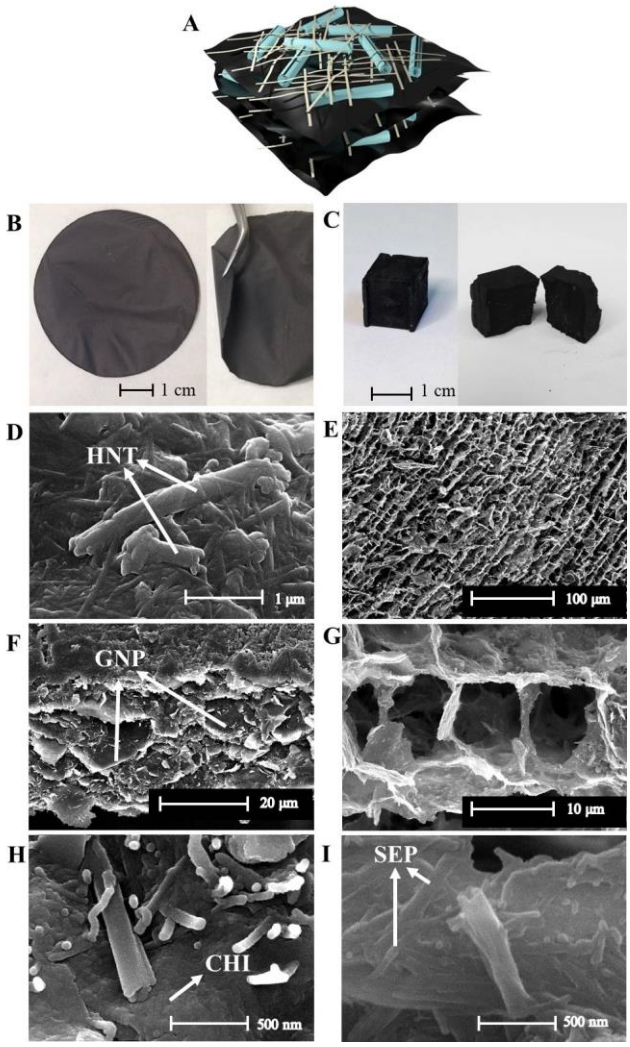

Figure 3. Schematic representation of particle assembly in the multicomponent bionanocomposites: A) cross-section of processed materials: HNT and SEP are represented as tubes and fibres, while chitosan, GNP and MWCNT are pictured in the black matrix. Photographs of B) Film-1 and C) Foam-1. SEM micrographs of the film: D) upper surface, F) and H) cross-section; SEM micrographs of the foam: E) and G) pore architecture, I) cell walls.

The porosity of the foams was estimated from their relative density values (Table 1). It was found that foams with high content of chitosan showed the lowest porosity, i.e. 89 vs. 96 % for low chitosan content. In fact, by reducing the chitosan content (and concomitantly increasing the clay and GNP content) the apparent density slightly decreases, while the skeletal density increases due to the higher density of the solid components. Consequently, the relative density decreases and the porosity increases. It is interesting to note that the foam structure does not seem to collapse by reducing the polymer content, which would be otherwise manifested in higher

apparent density values. The increased apparent density of the foams at higher chitosan content might be attributed to the tendency of the polymer matrix to create a more compact assembly of the particulate components [40-41].

Table 1. Apparent, skeletal, and relative density together with the corresponding porosity of the bionanocomposite foams.

Samples	NC[a] (wt%)	GNP[b] (wt%)	Chitosan (wt%)	ρ_{app}[c] (g cm^{-3})	ρ_{sc}[d] (g cm^{-3})	ρ_{rel}[e] (g cm^{-3})	Porosity %
Foam-1	18	55	15	0.071	1.9	0.04	96
Foam-2	12	36	45	0.072	1.4	0.05	95
Foam-3	10	30	54	0.076	1.2	0.06	94
Foam-4	6	18	72	0.080	0.7	0.1	89
Foam-5	2	6	91	0.081	0.4	0.21	79

[a] The ratio between both clay minerals (SEP:HNT) was kept at 1:1

[b] The ratio between both nanocarbons (GNP:MWCNT) was kept at 5:1.

[c] ρ_{app} denotes the apparent density.

[d] ρ_{sc} denotes the skeletal density.

[e] ρ_{rel} denotes the relative density calculated as ρ_{app}/ρ_{sc}.

The high porosity is also reflected in the nitrogen adsorption/desorption isotherms (Fig S2a, b). The BET specific surface area of the Film-1 and Foam-1 samples was 5 and 58 $m^2\ g^{-1}$, respectively.

The microstructure of the films was characterized by X-ray diffraction (XRD). The diffractogram of Film-1 displays the main reflections of both nanoclays and GNP without 2θ displacement (Figure S3). This suggests that here no intercalation of chitosan into the halloysite interlayer spacing occurred, conversely to other polymer-HNT composites and thus, halloysite still remains in its dehydrated form (Figure S4) [28, 32]. Furthermore, a change in the relative intensity of the main halloysite reflections is observed as a typical consequence of the instauration of a preferential in-plane orientation of the nanotubes in the film architecture (Figure S4 and see Supplementary Discussion) [42].

The mechanical properties of the bionanocomposite materials were evaluated in stress-strain measurements (Figure S5), analysing the influence of the nanofiller content on the elastic behaviour as in related biopolymer-based nanocomposites

[24]. The results show that the Young's modulus of the films (Figure 4A) increases with the clay nanofiller content from 5 GPa for pure chitosan up to 11 GPa for the Film-4 sample containing 40 % of clay components. These findings are in good agreement with the mechanical properties of similar composite materials based on sepiolite, MWCNT and poly(vinyl alcohol) [23], sepiolite, graphene nanoplatelets, and biopolymers (e.g., alginate, gelatine) [24] and cellulose or foams of microfibrillated cellulose and starch [43], which are in the range of 0.1-9 GPa.

The high stiffness of these materials has been previously attributed to the sepiolite fibres that strongly interact with chitosan chains and may also interlock physical movement and sliding of the other particulate components [44].

The mechanical testing (Fig 4B) of the bionanocomposite foams confirmed the crucial role of the chitosan matrix conferring robustness to these systems as the Young's modulus of 0.2 MPa for a foam without chitosan (with the composition of 1:1:1:0.3 in HNT/SEP/GNP/MWCNT) increases to 3.5 MPa after incorporation of the biopolymer (45 wt%). This tendency can be correlated to the strong interactions between the chitosan matrix and the sepiolite fibres as well as to an increase in the relative density that produces a decrease in porosity, commonly related to a smaller pore size and a lower tendency to collapse as in case of larger macropores [44, 45]. In contrast, a decrease in the compression modulus (1.4 MPa) was found for the sample with a higher content of chitosan (72 %), suggesting a synergic effect of both clays as reinforcing fillers of the polymer and as adhesive agent, which is required to improve the mechanical properties for the designed samples [46-47]. The obtained compression modulus is comparable to values measured for other chitosan/clay foams (1.4 MPa) [47] and significantly higher than those of self-assembled graphene hydrogels (0.03-0.3 MPa) [48]. Notably, the specific modulus of the bionanocomposite foams was 50 kNm kg^{-1}, which is considerably higher than values reported for silica aerogels (5–20 kNm kg^{-1}) [49] and is on par with polystyrene foams (10–100 kNm kg^{-1}) [45] and other bionanocomposite graphene-clay foams (77 kNm kg^{-1}) [39].

High electrical conductivity of the bionanocomposite films and foams is crucial for their application in electro-chemical devices, which was therefore assessed by the van der Pauw method. Figure 4C displays the in-plane electrical conductivity of the films as a function of the MWCNT content (composition of samples in Table 2).

Table 2. Composition and nomenclature of the prepared samples.

	Samples	wt% HNT	wt% SEP	wt% GNP	wt% MWCNT	wt% CHI
Films	Film-1[a)]	11	11	55	5	18
	Film-2	14	14	40	4	28
	Film-3	18	18	30	3	31
	Film-4	20	20	20	2	38
Foams	Foam-1[a)]	9	9	55	12	15
	Foam-2	6	6	36	7	45
	Foam-3	5	5	30	6	54
	Foam-4	3	3	18	4	72
	Foam-5	1	1	6	1	91

The sepiolite (SEP)-halloysite (HNT) ratio was kept at 1:1. GNP=graphene nanoplatelets, MWCNT=multiwalled carbon nanotubes, CHI=chitosan.

[a)] GOx loaded into HNT for biosensor and EBC assays.

A remarkable value of 2900 S m^{-1} is obtained at 5 wt% of carbon nanotubes, while the percolation threshold for electrical conductivity is at 4 wt% MWCNT content. The conductivity values are higher than the values reported previously for sepiolite-nanocarbon-polymer bionanocomposites, i.e. 1000-2500 S m^{-1} [13-14]. The high in-plane conductivity found here can be attributed to a synergic effect of MWCNT and the lamellar assembly of graphene nanoplatelets in the plane of the film as observed by SEM (see Figure 3F). The MWCNT act as nanowires connecting GNP particles, which facilitates the electron percolation across the insulating network of polymer and clays components [24, 27]. In addition, the polymer matrix appears to have a significant influence on the electrical conductivity. For similar GNP/MWCNT content bionanocomposites with different polymer matrices showed ca. 2700 S m^{-1} for alginate, 900 S m^{-1} for gelatin, and 300 S m^{-1} for poly(vinyl alcohol), while in the present case the chitosan matrix enabled a conductivity of 2900 S m^{-1} [24]. The increase of the conductivity in chitosan films can tentatively be ascribed to the presence of physically adsorbed water not only on the nanoclay surfaces but also associated with the polymer matrix favouring the transport of the electrical signal by ionic species including proton diffusion [50-51].

The electrical conductivity of the bionanocomposite foams is presented in Figure 4D. The foams displayed conductivity values of ca. 4.5 S m^{-1}, which is significantly lower as compared to the films of similar composition. This is attributable to the higher porosity and separation of the charge carriers. However, the electrical conductivity of these foams is considerably higher as compared to other related graphene-based foams (e.g. 0.5 S m^{-1}) [48]. The electrical percolation threshold of the foams was around 6.5 wt% MWCNT content. The higher value in foams reflects a poorer connectivity between carbon nanoparticles dispersed in the clays-polymer matrix probably enhanced by the high porosity, requiring thus a larger amount of GNP/MWCNT to form a conducting network within the matrix of the bionanocomposite. In any case, the percolation threshold is on par or slightly lower than the values for related MWCNT-polymer composites, which are in the range of 4-9 wt% [52-53].

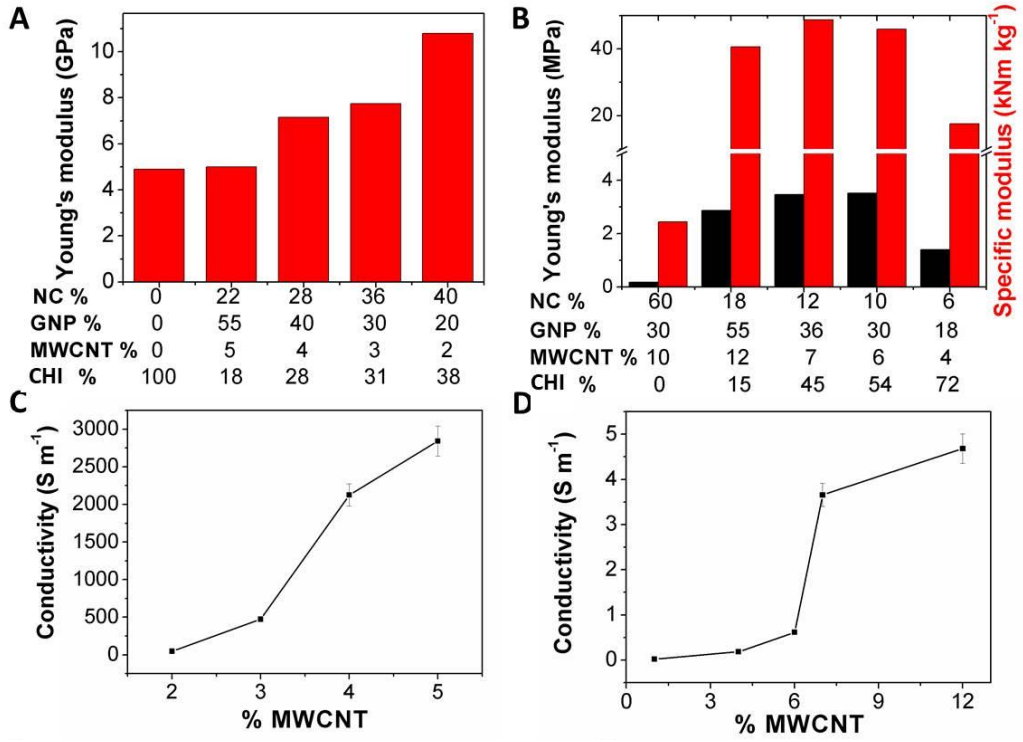

Figure 4. Young's moduli and electrical conductivity of HNT/SEP/GNP/MWCNT/CHI films (A, C) and foams (B, D), respectively.

The Film-1 bionanocomposite was used to evaluate the stability of these multicomponent hybrid materials in water showing a mass loss of only 3.2 wt% over the course of two months. This excellent stability, together with the good electrical and mechanical properties, suggests that the prepared multicomponent

bionanocomposite can be suitable as electrode material in aqueous medium. Moreover, the successful incorporation of HNT as nanoreactor prompted the use of these bionanocomposite materials in bioelectrocatalysis applications (*vide infra*).

Immobilization of glucose oxidase in the lumen of HNT

The developed multicomponent bionanocomposites were used for immobilization of the glucose oxidase enzyme in the search of multifunctional properties of interest in bioelectrochemical applications. GOx was chosen as a prototypic bioactive component because of its properties and compatibility with HNT that presents appropriate size (5.4 nm) as well as an appropriate isoelectric point (at pH ~ 4-4.5) for inclusion and immobilization on the surface of the halloysite lumen. Then, the presence of HNT was exploited as nanocontainer of GOx, avoiding the direct interaction of this protein with sepiolite fibres that may lead to enzymatic inactivity [54-55]. In fact, assays showed a drastic loss of enzymatic activity when GOx was incorporated in the film without previous immobilization within HNT. Hence, GOx was immobilized in the HNT clay prior to its incorporation in the multicomponent mixture. The uptake of GOx was 7.7 ± 0.2 wt% according to CHN elemental analysis. The enzyme immobilization was also confirmed by FTIR spectroscopy (Figure S6 and Table S1), the HNT-GOx spectrum clearly showing the presence of bands assigned to symmetric stretching of C-H aliphatic group and amide groups of GOx [56]. In particular, there is no significant variation in the amide I and II vibrations of the immobilized GOx enzyme with respect to unsupported GOx. This observation strongly supports that the adsorption of GOx in HNT occurs via non-deteriorating electrostatic interactions [53]. This physical entrapment, in contrast to immobilization via covalent bonding is essential for the preservation of the enzyme structure and bioactivity [35, 54].

The presence of GOx in the HNT lumen was also evidenced from nitrogen adsorption–desorption isotherms (Fig S7). Compared to pristine HNT, a notable decrease of the specific surface area from 25 to 19 m^2 g^{-1} for HNT-GOx could be observed. The volume of the mesopores was also reduced after GOx uptake (Table S2) in agreement with a partial pore blockage, supporting the hypothesis that the majority of GOx was loaded into the HNT lumen [22].

With the GOx loaded HNT a multicomponent bionanocomposite film (Film-GOx) and foam (Foam-GOx) were prepared with the composition of Film-1 and Foam-1,

respectively (see Table 2). The enzymatic activity of the Film-GOx was confirmed in a test with peroxidase and ABTS, indicating that the preparation procedure did not affect the response of the entrapped GOx towards glucose (Figure S8).

Application of film-GOx as biosensor in glucose detection.

The GOx loaded bionanocomposite film (Film-GOx) was tested as biosensor for the detection of glucose (scheme in Figure 5A). The performance of the biosensor was studied by cyclic voltammetry (CV) in the presence of potassium ferricyanide as mediator, relying on the mediated electron transfer (MET) mechanism. Figure 5B shows the CV curve of the biosensor in response to 50 mM glucose in phosphate buffered solution (PBS). The intensity of the oxidation and reduction peaks of $Fe(CN6)^{4-}$ at 0.19 and 0.33 V, respectively, increases significantly in presence of glucose. Together with the change of the CV curve shape this confirms the catalytic behaviour of the immobilized enzymes [57-58]. The steady-state current *vs.* glucose concentration is depicted in Figure 5C showing the Michaelis–Menten behaviour, i.e. the effect of substrate concentration on the rate of the enzyme-catalysed reaction. The use of potassium ferricyanide as mediator enabled a fast electron transfer between the enzyme and the electrode surface. In fact, fitting of the curve with the Lineweaver–Burk plot (Figure S9) rendered a Michaelis–Menten constant (Km) of 9.3 mM, which is smaller than those reported for GOx in solution (33 mM) [58] and GOx immobilized in mesopores of Al_2O_3 membranes (10-30 mM) [59], sol–gel-derived composite films (14 mM) [60], and similar devices based on graphene and carbon nanotubes (4-15 mM) [61-62]. The low Km value is indicative of excellent performance attributed to a strong ability toward substrate binding and high enzymatic activity of the immobilized GOx [61].

The linear range of the biosensor was 0-1.1 mM glucose and the sensitivity was as high as 34 µA mM^{-1}. These results also reflect the stronger response of the designed biosensor to low amounts of glucose with respect to other devices based on immobilized GOx on, for instance, graphene, CNT, and buckypapers (10-25 µA mM^{-1}) [46, 62-63], the external surface of functionalised HNT (5.2 µA mM^{-1}) [19], polymeric (5 µA mM^{-1}) [64] or chitosan modified matrix (1.2 µA mM^{-1}) [65].

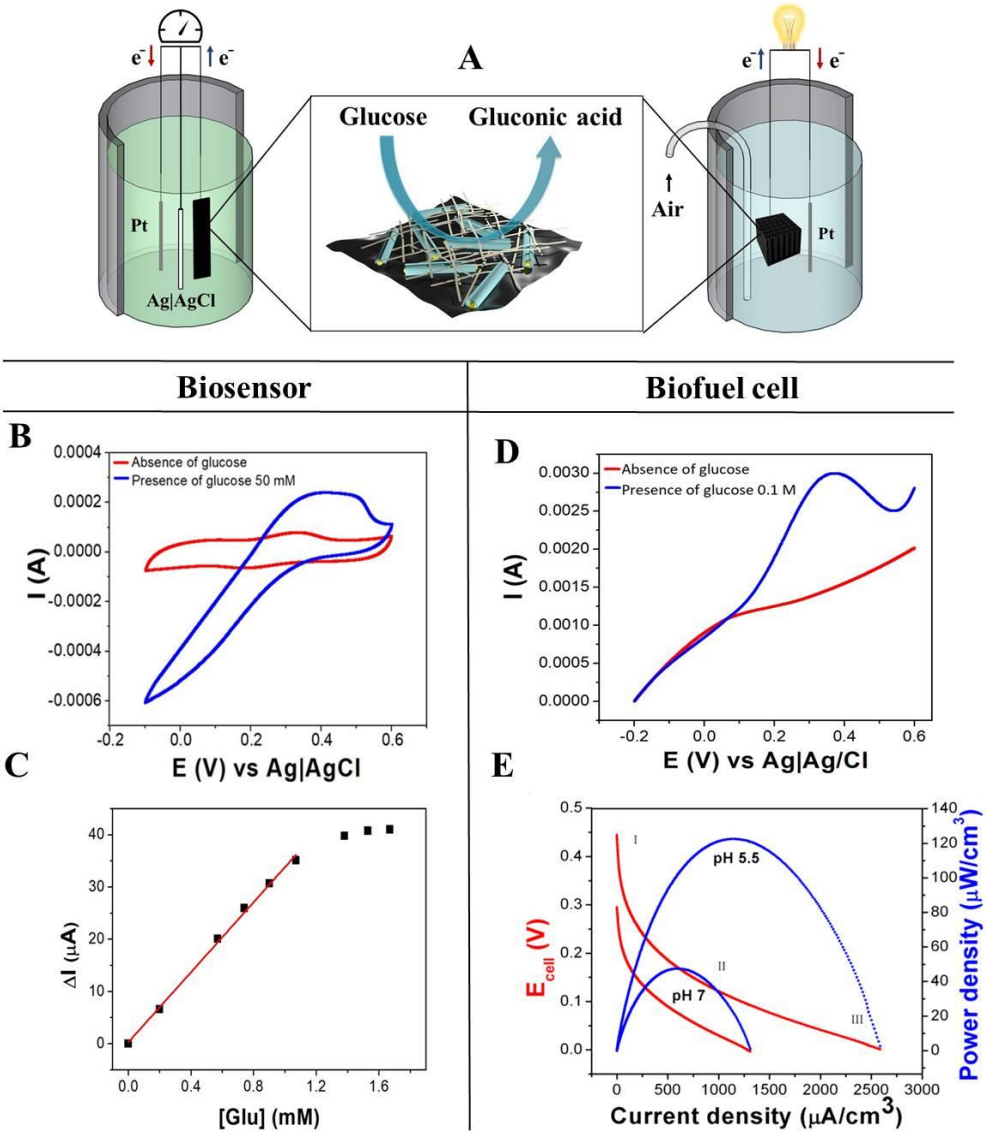

Figure 5. A) Scheme of EBC (left) and biosensor (right) with the electrode microstructure and biocatalytic oxidation of glucose at the bioactive nanocomposite interface. B) Effect of glucose on the Film-GOx sample with CV measurement in PBS, pH 7 and 0.1 mM of ferricyanide at a scan rate of 5 mV s^{-1}. C) Sensor response as a function of glucose concentration. The red line is a linear fit. ΔI = steady-state current at 0.45 V. D) LSV measurement of Foam-GOx immersed in PBS at pH=7 and in the presence of glucose 0.1 M in PBS at the same pH. E) Polarization curve obtained by LSV measurement at a scan rate of 1 mV s^{-1}. The medium is a PBS with glucose 1 M at pH 7 and pH 5.5.

The crucial role of HNT as protective container for the enzymes was underlined by immobilizing GOx directly on bionanocomposite films prepared without incorporation of halloysite, where the enzyme was directly integrated in the system after the ultrasonication treatment. The CV curves of these films showed no response to

glucose (Figure S10), suggesting the inactivity of the entrapped enzyme. This is probably due to the direct interaction of the enzyme with sepiolite. It is well known that the electrostatic interaction of proteins with the external surface of sepiolite can be very strong and, in some cases, might cause the inactivity of the biological functionality [56].

Application of foam-GOx as bioanode in a membrane-less and open-air biofuel cell

It is well-known that redox mediators are required for most of the GOx based bioelectrocatalysis applications to guarantee an efficient electron transfer process from the enzyme to the electrode interface [66]. Therefore, in a preliminary assay the Foam-GOx was tested in presence of $Fe(CN_6)^{4-}$ mediator and separated from the cathode chamber by a Nafion® membrane, which generated a power density of 565 $\mu W\ cm^{-3}$ and 31 $\mu W\ cm^{-2}$ (Figure S11). Next, the enzymatic biofuel cell (EBC) performance was evaluated in open-air condition and in the absence of any mediator or expensive proton exchange membranes (e.g. Nafion®). Figure 5A illustrates the EBC designed as a one-pot cell. The GOx enzyme catalyses the conversion of glucose in gluconic acid as in the following [67]:

$$\text{FAD-GOx} + \text{Glucose} \rightarrow \text{FADH}_2\text{-GOx} + \text{Gluconic acid} \qquad (1)$$

The reaction occurring on the bioanode surface is:

$$\text{FADH}_2\text{-GOx} \rightarrow \text{FAD-GOx} + 2H^+ + 2e^- \qquad (2)$$

while the Pt cathode catalyses the reaction:

$$O_2 + 4H^+ + 4e^- \rightarrow 2H_2O \qquad (3)$$

Linear sweep voltammetry (LSV) experiments were carried out to evaluate the electrocatalytic properties of the bionanocomposite Foam-GOx as 3D bioanode. Figure 5D displays the catalytic behaviour towards glucose oxidation. In fact, with the addition of 0.1 M glucose, a clear increase (blue line) of the anodic current appears compared to that in PBS without glucose. For the here designed mediator-less cell, this behaviour is correlated to a direct electron transfer (DET) at the interface between the active site (FAD) of the enzyme and the conducting elements of the

electrode surface, confirming that a DET mechanism is involved [68-69]. The current increase is predominant at a voltage of 0.35 V, which is higher than the typical FAD/$FADH_2$ standard voltage (i.e., −0.460 V in pH 7.0 at 25.8 °C) probably due to the presence of carbon nanotubes that can influence the electrochemical response [56].

The polarization measurements were carried out in a concentrated glucose solution (1 M) to estimate the maximum power density regardless of the glucose content [66-67]. The polarization curves for the described biofuel cell working at two different pH values are shown in Figure 5E. The polarization curves show the common behaviour of microbial fuel cells (MFCs) and EBCs and it can be divided into three zones: I, II and III as shown in Figure 5E, conventionally called the activation zone, ohmic losses, and the mass transport zone [68-69].

The open circuit potential (OCP) of the cell at pH of 5.5 was 0.442 V, while at pH 7 the OCP was 0.298 V. This finding can be correlated to the combination of effects such as a better working pH for the glucose oxidase (the optimal working pH of GOx is closed to 5) and a faster oxygen reduction at the cathode surface. The presence of the acidic medium, in fact, can favour the proton migration from the anode to the cathode surface leading to the increase of half-cell potential [66]. Concerning the power output the EBC showed different performance at the two pH values. Compared to pH=7 the cell working at pH=5.5 exhibits an increase in volumetric power density from 47.8 μW cm^{-3} at 0.081 V to 120 μW cm^{-3} at 0.116 V and current density from 1.3 mA cm^{-3} to 2.6 mA cm^{-3}, respectively, as well as a rise in surface power density from 2.6 μW cm^{-2} to 6.5 μW cm^{-2} respectively. These values are in good agreement with other EBC systems, indicating thus the good performance the Foam-GOx bionanocomposite (Table 3).

Table 3. Performance of diverse published EBFC systems utilizing DET or MET mechanism.

Anode	**Cathode**	**Mecha-nism**	**OCP (V)**	**Power density**	**Reference**
GOX-graphene/SWCNT cogel	BOD-graphene/SWCNT cogel	DET	0.61	190 μW cm^{-2} 650 μW cm^{-3}	Ref. 68
Graphite/GOx/catalase/ubiquinone	Graphite/PPO/quinhydrone	MET	0.27	24 μW cm^{-3}	Ref. 70

CNT/GOx/catalase	CNT/laccase	DET	0.57	193 μW cm^{-2} 161 μW cm^{-3}	Ref. 71
Fc-MeOH/GOx CNPs	ABTS2-/BOD CNPs	MET	0.5	95 μW cm^{-2}	Ref. 72
GOx/SWNT/Ppy composite	Tyrosinase/CNPs/Ppy composite	DET	-	158 μW cm^{-3}	Ref. 73
CDH/AuNPs	MvBOx/AuNPs	DET	0.57	1 μW cm^{-2}	Ref. 74
GMC/GOx/GA	Pt	DET	0.48	22 μW cm^{-2}	Ref. 75
CNTs/FcMe2-LPEI/Lactate	CNTs/Ar-pyr/ BOx	MET	0.44	2.4 μW cm^{-2}	Ref. 76
Foam-GOx	Pt	MET	0.32	31 μW cm^{-2} 565 μW cm^{-3}	This work
Foam-GOx	Pt	DET	0.44	6.5 μW cm^{-2} 120 μW cm^{-3}	This work

The decrease of power density compared to the cell working in presence of redox mediator is associated with a slower electron transfer at the enzyme-electrode interface. Nevertheless, the confined GOx in halloysite nanotubes was able to work even in DET mechanism, allowing the use also in a physiological environment [68, 70].

Furthermore, the high surface area promotes better contact between glucose and the active sites of the enzyme, but at the same time the high porosity of 96 % of the bioanode help to delay the leaching of bioactive components because, before being released into the aqueous medium, it must take a tortuous path through the pore system of the foam, supporting a good stability over time. A preliminary evaluation of this effect was carried out by repeating the test during 5 days working, storing the system in PBS at 30° C, observing the retention of 93 % of its initial power.

Conclusion

This work reports a preliminary proof of concept study showing the viability to integrate nanoclays, biopolymers, and graphene-based conducting components into homogeneous multifunctional nanoarchitectured materials. The presence of sepiolite

fibrous clay together with ultrasonication is the key to disperse all these components in water. The resulting stable colloids can be processed as films and foams displaying acceptable mechanical properties, good electrical conductivity, and controlled porosity useful for diverse applications at the nanoscale. HNT was efficiently loaded with 7.7 wt% of the model enzyme glucose oxidase that preserved high enzymatic activity inside the halloysite lumen. This allows the exploration of the multicomponent bionanocomposites as functional components of electrochemical devices such as biosensor and as 3D bioanode in a biofuel cell. The latter revealed a volumetric power density of 120 μW cm^{-3} and a good stability over time and temperature (the power density decreased only by 7 % after 5 days and storing at 30 °C). These bioelectrocatalysis results represent an incipient development that could be extended in the future to other fields of interest, especially considering the versatility of halloysite as nanocontainer of many diverse bioactive species [16]. On the other hand, the possibility to introduce additional functionalities by modification of sepiolite, for instance by incorporating magnetic or photoactive nanoparticles [7], could pave the way to further applications of these multicomponent functional bionanocomposites in the near future.

Experimental

Materials

Sepiolite (SEP) from the Vallecas-Vicálvaro clay deposits (Madrid, Spain) was provided by TOLSA S.A. (Spain) as a commercial, rheological grade product (Pangel® S9). This microfibrous clay has a low cationic exchange capacity (ca. 15 meq 100 g^{-1}) and high specific surface area (~ 300 m^2 g^{-1}). Dehydrated halloysite nanotubes (HNT) from the New Zealand China Clays deposits were provided by Imerys (France). Before use, HNT were ground and sieved through a 250 μm mesh. Glucose oxidase (GOx; type VII-S, 181.500 U g^{-1} solid; E.C.1.1.3.4 from Aspergillus niger) was supplied by Sigma-Aldrich. Graphene nanoplatelets (GNP) are multilayered graphene sheets that were supplied by KNANO (China) under the name of KNG-150. They are composed by more than ten carbon layers with 5–15 nm thickness and 1–20 μm diameter, showing electrical conductivity of 12 000 S m^{-1} and a specific surface area of 41 m^2 g^{-1} (according to the manufacturer). Multiwalled carbon nanotubes (MWCNT), with more than 95 % of carbon content, were obtained

from Dropsens S.A. (Spain) and used without further treatment. The average diameter of the tubes was 10 nm and the average length 1.5 µm. Acetic acid (~ 99.5 %) was obtained from Merck. d-Glucose anhydrous (99 %) was obtained from Scharlau. Peroxidase (HRP; type II, 120,000 U/g solid; E.C.1.11.1.7 from horseradish) were purchased from Sigma Chemical Co., whereas 2,2'-azino-bis(3-ethylbenzothiazoline-6-sulphonic acid) (ABTS) was obtained from Fluka. Sodium phosphate tribasic dodecahydrate, ~ 98 %, was furnished by Sigma and phosphoric acid (85 %) by Carlo Erba. Bi-distilled water (18.2 MΩ cm) was obtained from a Maxima Ultra Pure Water system from Elga. Chitosan with a medium molecular weight of 190-310 kDa, 75–85 % deacetylated, was obtained from Aldrich.

Preparation of starting colloidal suspensions and bionanocomposite films and foams

The scheme of the multicomponent bionanocomposites preparation is shown in Figure 1. Two sets of aqueous mixtures of chitosan (CHI) and different proportions (Table 2) of SEP/HNT/GNP/MWCNT were prepared at overall concentrations of 0.2 % w/v and 8 % w/v, respectively. First, the appropriate amounts of both nanoclays and GNP/MWCNT were dispersed in bi-distilled water and exposed to pulsed ultrasonic irradiation (VC750 Sonics Vibra-Cell, operating at 20 kHz) using a 13 mm standard probe. Separately, chitosan was slowly dissolved in an aqueous solution of 1 % v/v acetic acid at 70 °C and added to the SEP/HNT/GNP/MWCNT dispersion under magnetically stirring.

The bionanocomposite films were processed by solvent casting from the 0.2 % w/v dispersion on polyester Petri dishes and dried at 30 °C and 60 % relative humidity (RH) in a CLIMACELL EVO Stability Chamber (Incubator model 111L).

The bionanocomposite foams were prepared by freeze-drying (Cryodos-80, Telstar) of the 8 % w/v dispersion that was cast in cylindrical plastic containers and plunged in liquid nitrogen.

Immobilization of glucose oxidase in halloysite nanotubes and their incorporation in bionanocomposite matrices

Glucose oxidase (100 mg) was dissolved in water (1 ml) and mixed with HNT (200 mg). Then, the sample was vortexed and sonicated in an ultrasound bath until no

aggregates of halloysite were visible. To ensure complete infiltration of the HNT lumen by the GOx solution the samples were subject to alternating cycles of reduced pressure (approx. 70 mmHg). The loaded HNT-GOx were separated from the solution by centrifugation, washing and finally dried overnight in a desiccator at 30 °C and stored at 4 °C until usage. HNT-GOx was added to the SEP/GNP/MWCNT/CHI mixtures (0.2 % w/v and 8 % w/v) described above, obtaining compositions Film-1 and Foam-1, respectively (Table 1). The resulting suspensions were processed by solvent casting and freeze casting methods to obtain the bioactive films (film-GOx) and the bioactive foams (foam-GOx), respectively, and were stored at 4 °C until usage.

Characterization techniques

The morphology of the prepared bionanocomposite films and foams was evaluated by scanning electron microscopy (SEM) using a SEM Philips XL 30 S-FEG microscope. Before examination, the samples were fractured in liquid nitrogen. The FTIR spectra of HNT-GOx samples were acquired with a BRUKER iFS spectrophotometer 66Vs. X-ray diffractograms were obtained with a D8-ADVANCE diffractometer (Bruker), using Cu K_α radiation. The voltage and current sources were set at 40 kV and 30 mA, respectively. Diffractograms were recorded at a goniometer speed of 0.5 s per step between 4° and 60° (2θ). The BET specific surface area and the pore size distribution (Barret-Joyner-Hallenda (BJH) method) were determined from nitrogen adsorption/desorption isotherms obtained on a Micromeritics ASAP 2010 analyser. The samples were degassed at 120 °C under vacuum. The stability of the bionanocomposites in water was assessed by immersing a piece of the film in bi-distilled water for 2 months and noting the weight loss. The relative density (ρ_{rel}) of the bionanocomposite foams was estimated from the skeletal density using the following values: SEP = 2.3 g cm^{-3}, HNT = 2.2 g cm^{-3}, GNP = 2.3 g cm^{-3}, MWCNT = 2.1 g cm^{-3}, Chitosan = 0.2 g cm^{-3}. The mechanical properties of the films and foams were assessed at ambient conditions by using an universal test machine (Instron Model 3345) equipped with a 5 kN load cell and at 1 mm min^{-1} frame speed. At least three measurements were performed per sample. The electrical conductivity was determined by the four-point method, using a Solartron 1480 potentiostat (MultiStat). Elemental chemical analysis (CNHS Perkin Elmer 2400 analyzer) was carried out to estimate the amount of loaded GOx in HNT.

Biosensing test.

Cyclic voltammetry (CV) was performed with a standard three-electrode electrochemical cell connected to a Solartron 1480 MultiStat potentiostat. Platinum wire was used as a counter electrode and Ag|AgCl (soaked in 1.0 M KCl) was used as a reference electrode. In the biosensing tests, the working electrode was a film of 30 × 5 mm × 0.014 (3.49 mg, containing 0.028 mg of immobilized GOx) immersed in a potassium ferricyanide solution (0.2 mM) as mediator containing 0.1 M of phosphate buffered solution (PBS, pH=7). CV was performed in a potential range of -0.2 to 0.6 V at a scan rate of 5 mV s^{-1}.

Biofuel cell test

Polarization curves were obtained from linear sweep voltammetry (LSV) performed with a μStat 100 potentiostat (Dropsens, Spain) in a two electrodes configuration. The glucose/air biofuel cell was assembled by coupling the bioactive foam, as anode, to a Pt wire as cathode in a one-pot cell working in 0.1 M of glucose and 0.1 M PBS, at two different pH values (7 and 5.5) and saturated by air. The foam was connected to the potentiostat with a copper wire, glued with colloidal graphite and covered by an epoxy resin as isolating material. All tests were run three times at a scan rate of 1 mV s^{-1} starting from the open circuit potential (OCP, I=0) to the short-circuit cell voltage ($I=I_{max}$). From the V_{cell} *vs.* I data, the power (P) was calculated by Equation 1.

$$P = I \times V_{cell} \quad (1)$$

Finally the power density was obtained as a surface power density (μW cm^{-2}), since the roughness factor (ECSA) calculated from the CV measurements and as a volumetric power density (μW cm^{-3}) considering as volume a specific volume (0.02 cm^3), calculated from the specific density (1.9 g cm^{-3}) [27].

Supporting Information

Supporting Information File 1: Lo Dico et al. Supporting info.docx

Acknowledgements

The authors thank the MINECO (project MAT2015-71117-R) for financial support. GLD and LL acknowledge the University of Palermo for the “UOB21 Borse di studio finalizzate alla ricerca” grants. BW thanks the MINECO for an IJCI contract (IJCI-2015-23886).The authors also thank Dr. M. Darder, Dr. M.L. Ferrer, and Dr. N. López-Salas for fruitful discussions on bioelectrocatalysis.

References

1. Aono, M.; Bando, Y.; Ariga, K. Nanoarchitectonics: Pioneering a New Paradigm for Nanotechnology in Materials Development. *Adv. Mater.* **2012**, *24*, 150–151.
2. Ariga K. (Ed.). Manipulation of Nanoscale Materials: An Introduction to Nanoarchitectonics, *Royal Society of Chemistry*, Cambridge (UK), **2012**.
3. Komiyama, M.; Yoshimoto, K.; Sisido, M.; Ariga, K. Chemistry Can Make Strict and Fuzzy Controls for Bio-Systems: DNA Nanoarchitectonics and Cell-Macromolecular Nanoarchitectonics. *Bull. Chem. Soc. Jpn.* **2017**, *90*, 967.
4. Khan, A. H.; Ghosh, S.; Pradhan, B.; Dalui, A.; Shrestha, L. K.; Acharya, S.; Ariga, K. Two-Dimensional (2D) Nanomaterials towards Electrochemical Nanoarchitectonics in Energy-Related Applications. *Bull. Chem. Soc*. Jpn. **2017**, *90*, 627.
5. Ariga, K.; Mori, T.; Shrestha, L.K. Nanoarchitectonics from Molecular Units to Living-Creature-Like Motifs. *Chem. Rec*. **2018**, *18*, 676–695.
6. Ruiz-Hitzky, E.; Aranda, P.; Belver, C. Manipulation of Nanoscale Materials: An Introduction to Nanoarchitectonics (Ed.: K. Ariga). *Royal Society of Chemistry*, Cambridge (UK), **2012**, 89–111.
7. Aranda, P.; Ruiz-Hitzky, E. Immobilization of nanoparticles on fibrous clay
Surfaces: towards promising nanoplatforms for sdvanced functional applications.
Chem. Rec. **2018**, *18*, 1125.

8. Vinokurov, V.A.; Stavitskaya, A.V.; Glotov, A.P.; Novikov, A.A.; Zolotukhina, A.V.; Kotelev, M.S.; Gushchin, P.A.; Ivanov, E.V.; Darrat, Y.; Lvov, Y.M. Nanoparticles formed onto/into halloysite clay tubules: architectural synthesis and applications. *Chem. Rec*. **2018**, 18, 858–867.
9. Glotov, A.; Levshakov, N.; Stavitskaya, A.; Artemova, M.; Gushchin, P.; Ivanov, E.; Vinokurov, V.; Lvov, Y. Templated self-assembly of ordered mesoporous silica on clay nanotubes, *Chem. Commun*. (in press)
10. Li, L.; Ma, W.; Higaki, Y.; Kamitani, K.; Takahara, A. Organic−Inorganic Hybrid Thin Films Fabricated by Layer-by-Layer Assembly of the Phosphorylated Cellulose Nanocrystal and Imogolite Nanotubes, *Langmuir*, **2018**, *34*, 13361−13367.
11. Liangjie, F.; Huaming, Y.; Aidong, T.; Yuehua, H. Engineering a tubular mesoporous silica nanocontainer with well-preserved clay shell from natural halloysite. *Nano Res.* **2017**, *10*, 2782.
12. Lazzara, G.; Cavallaro, G.; Panchal, A.; Fakhrullin, R.; Stavitskaya, A.; Vinokurov, V.; Lvov, Y. An assembly of organic-inorganic composites using halloysite clay nanotubes. *Curr. Opin. Colloid Interface Sci.* **2018**, *35*, 42.
13. Lvov, Y.; Wang, W.; Zhang, L.; Fakhrullin, R. Halloysite Clay Nanotubes for Loading and Sustained Release of Functional Compounds. *Adv. Mater.* **2016**, *28*, 1227.
14. Cavallaro, G.; Lazzara, G.; Milioto, S.; Rozhina, E.; Fakhrullin, R.; Nanohydrogel formation within the halloysite lumen for triggered and sustained release. *ACS Appl. Mater. Interfaces* **2018**, *10*, 8265.
15. Lo Dico, G.; Semilia, F.; Milioto, S.; Parisi, F.; Cavallaro, G.; Inguì, G.; Makaremi, M.; Pasbakhsh P.; Lazzara, G. Microemulsion Encapsulated into Halloysite Nanotubes and their Applications for Cleaning of a Marble Surface, *Applied Science*, **2018**, *8*, 1455.
16. Tully, J.; Yendluri, R.; Lvov, Y.; Halloysite clay nanotubes for enzyme immobilization. *Biomacromolecules* **2016**, *17*, 615.
17. Lvov, Y.; Shchukin, D. G.; Mohwald, H.; Price, R. Halloysite clay nanotubes for controlled release of protective agents. *ACS Nano* **2008**, *2*, 814.
18. Shchukin, D. G.; Sukhorukov, G. B.; Price, R. R.; Lvov, Y.; Halloysite nanotubes as biomimetic nanoreactors. *Small* **2005**, *1*, 510.
19. Kumar-krishnan, S.; Hernandez-Rangel, A.; Pal, U.; Ceballos-Sanchez, O.; FloresRuiz, F. J.; Prokhorov, E.; De Fuentes, O. A.; Esparza, R.; Meyyappan, M.

Surface functionalized halloysite nanotubes decorated with silver nanoparticles for enzyme immobilization and biosensing. *J. Mater. Chem. B* **2016**, *4(15)*, 2553.
20. Sun, X.; Zhang, Y.; Shen, H.; Jia, N. Direct electrochemistry and electrocatalysis of horseradish peroxidase based on halloysite nanotubes/chitosan nanocomposite film. *Electrochim. Acta*, **2010**, *56*, 700.
21. Cavallaro, G.; Lazzara, G.; Milioto, S. Exploiting the colloidal stability and solubilization ability of clay nanotubes/ionic surfactant hybrid nanomaterials. *J. Phys. Chem. C*, **2012**, *116*, 21932.
22. Pasbakhsh, P.; Jock, G.; Natural mineral nanotubes, properties and applications. *Apple Academic Press Inc.* **2015**.
23. Fernandes, F. M.; Ruiz-Hitzky, E. Assembling nanotubes and nanofibers: Cooperativeness in sepiolite–carbon nanotube materials. *Carbon* **2014**, *72*, 296.
24. Ruiz-Hitzky, E.; Sobral, M. M. C.; Gómez-Avilés, A.; Nunes, C.; Ruiz-García, C.; Ferreira, P.; Aranda, P. Clay-graphene nanoplatelets functional conducting composites. *Adv. Funct. Mater.* **2016**, *26*, 7394.
25. Ruiz-Hitzky, E. Molecular access to intracrystalline tunnelsof sepiolite. *J. Mater. Chem.* **2001**, *11*, 86.
26. Ruiz-Hitzky, E.; Darder, M.; Alcântara, A. C. S.; Wicklein, B.; Aranda, P. Functional nanocomposites based on fibrous clays. *RSC Smart Mater.* **2017**, *22*, 1.
27. Del Campo, M. M. G.; Darder, M.; Aranda, P.; Akkari, M.; Huttel, Y.; Mayoral, A.; Bettini, J.; Ruiz-Hitzky, E. Functional hybrid nanopaper by assembling nanofibers of cellulose and sepiolite. *Adv. Funct. Mater.* **2018**, *28*, 1703048.
28. Bertolino, V.; Cavallaro, G.; Lazzara, G.; Merli, M.; Milioto, S.; Parisi, F.; Sciascia, L. Effect of the biopolymer charge and the nanoclay morphology on nanocomposite materials. *Ind. Eng. Chem. Res.*, **2016**, *55*, 7373.
29. Makaremi, M.; Pasbakhsh, P.; Cavallaro, G.; Lazzara, G.; Aw, Y. K.; Lee, S. M.; Milioto, S. Effect of morphology and size of halloysite nanotubes on functional pectin bionanocomposites for food packaging applications. *ACS Appl. Mater. Interfaces* **2017**, *9*, 17476.
30. Wang, Y.; Qi, W.; Huang, R.; Su, R.; He, Z. Counterion-Directed, structurally tunable assembly of hydrogels, membranes, and sacs at aqueous liquid–liquid interfaces. *Adv. Mater. Interfaces* **2016**, *3*, 1500327.

31. Deuber, F.; Mousavi, S.; Federer, L.; Adlhart, C. Amphiphilic nanofiber based aerogels from electrospun biopolymers for selective liquid absorption. *Adv. Mater. Interfaces* **2017**, *4* 1700065.
32. Sun, J.; Yendluri, R.; Liu, K.; Guo, Y.; Lvov, Y.; Yan, X. Enzyme-immobilized clay nanotube–chitosan membranes with sustainable biocatalytic activities. *Phys. Chem. Chem. Phys.* **2017**, *19*, 562.
33. Yanbing, Y.; Xiangdong, Y.; Yaning, T.; Quan, Y. Recent progress in flexible and wearable bio-electronics based on nanomaterials. *Nano Res.* **2017**, *10(5),* 1560.
34. Ghimire, A.; Pattammattel, A.; Maher, C. E.; Kasi, R. M.; Kumar, C. V. Three-dimensional, enzyme biohydrogel electrode for improved bioelectrocatalysis. *ACS Appl. Mater. Interfaces* **2017**, *9*, 42556.
35. Kang, Z.; Jiao, K.; Yu, C.; Dong, J.; Peng, R.; Hu, Z.; Jiao, S. Direct electrochemistry and bioelectrocatalysis of glucose oxidase in CS/CNC film and its application in glucose biosensing and biofuel cells. *RSC Adv.* **2017**, *7*, 4572.
36. Tiwari, N. J.; Vij, K. V.; Kemp, C.; Kwang, S. K. Engineered carbon-nanomaterial-based electrochemical sensors for biomolecules. *ACS Nano* **2016**, *10*, 46.
37. Voiry, D.; Chhowalla, M.; Gogotsi, Y.; Kotov, N. A.; Li, Y.; Penner, R. M.; Schaak, R. E.; Weiss, P. S. Best practices for reporting electrocatalytic performance of nanomaterials. *ACS Nano* **2018**, *12*, 9635.
38. Wicklein, B.; Diem, A. M.; Knöller, A.; Cavalcante, M. S.; Bergström, L.; Bill, J.; Burghard, Z. Dual-fiber approach toward flexible multifunctional hybrid materials. *Adv. Funct. Mater.* **2017**, *2*, 1704274.
39. Wicklein, B.; Kocjan, A.; Salazar-Alvarez, G.; Carosio, F.; Camino, G.; Antonietti, M. Bergström, L. Thermally insulating and fire-retardant lightweight anisotropic foams based on nanocellulose and graphene oxide, *Nat Nanotechnol* **2015**, *10*, 277.
40. Yan, J.; Wu, T.; Ding, Z.; Li, X. Preparation and characterization of carbon nanotubes/chitosan composite foam with enhanced elastic property. *Carbohydr Polym* **2016**, *136*, 1288.
41. Wu, Y.; Wang, Z.; Liu, X.; Shen, X.; Zheng, Q.; Xue, Q.; Kim, J. *ACS Appl. Mater. Interfaces* **2017**, *9*, 9059.
42. Żbik, M. S.; Raftery, N. A.; Smart, R. S. C.; Frost, R. L. Kaolinite platelet orientation for XRD and AFM applications. *Appl. Clay Sci.* **2010**, *50*, 299.

43. Svagan, A. J.; Berglund, L. A.; Jensen, P. Cellulose nanocomposite biopolymer foam—hierarchical structure effects on energy absorption. *ACS Appl. Mater. Interfaces* **2011**, *3*, 1411.
44. Darder, M.; López-Blanco, M.; Aranda, P.; Aznar, A. J.; Bravo, J.; Ruiz-Hitzky, E. Microfibrous Chitosan-Sepiolite Nanocomposites. *Chem. Mater.* **2006**, *18*, 1602.
45. Gibson, L. J.; Ashby, M. F. Cellular Solids: Structure and Properties. *Cambridge Univ. Press* **1999**.
46. Wicklein, B.; Aranda, P.; Ruiz-Hitzky, E.; Darder, M. *J.* Hierarchically structured bioactive foams based on polyvinyl alcohol–sepiolite nanocomposites. *Mater. Chem. B* **2013**, *1*, 2911.
47. Padilla-Ortega, E.; Darder, M.; Aranda, P.; Figueredo Gouveia, R.; Leyva-Ramos, R.; Ruiz-Hitzky, E. Ultrasound assisted preparation of chitosan–vermiculite bionanocomposite foams for cadmium uptake. *Appl. Clay Sci.* **2016**, *130*, 40.
48. Xu, Y.; Sheng, K.; Li, C.; Shi, G. Self-assembled graphene hydrogel via a one-step hydrothermal process. *ACS Nano*, **2010**, *4*, 4324.
49. Obrey, K. A. D.; Wilson, K. V.; Loy, D. A. *J.* Enhancing mechanical properties of silica aerogels. *Non-Cryst. Solids* **2011**, *357*, 3435.
50. Shaari, N.; Kamarudin, S. K. *J.* Chitosan and alginate types of bio-membrane in fuel cell application: An overview. *Power Sources* **2015**, *289*, 71.
51. Bai, H.; Zhang, H.; He, Y.; Liu, J.; Zhang, B.; Wang, J. Enhanced proton conduction of chitosan membrane enabled by halloysite nanotubes bearing sulfonate polyelectrolyte brushes. *J. Memb. Sci.* **2014**, *454*, 220.
52. Vasileiou, A. A.; Kontopoulou, M.; Gui, H.; Docoslis, A. correlation between the length reduction of carbon nanotubes and the electrical percolation threshold of melt compounded
polyolefin composites. *ACS Appl. Mater. Interfaces* **2015**, *7*, 1624.
53. Vasileiou, A. A.; Docoslis, A.; Kontopoulou, M.; Xiang, P.; Ye, Z. The role of non-covalent interactions and matrix viscosity on the dispersion and properties of LLDPE/MWCNT nanocomposites. *Polym.* **2013**, *54*, 5230.
54. Wicklein, B.; Darder, M.; Aranda, P.; Ruiz-Hitzky, E. Phospholipid–Sepiolite Biomimetic Interfaces for the Immobilization of Enzymes. *ACS Appl. Mater. Interfaces* **2011**, *3*, 4339.

55. Wicklein B.; Martín del Burgo M. Á.; Yuste M.; Darder M.; Llavata C. E.; Aranda P.; Ortin J.; Del Real G.; Ruiz-Hitzky E. Lipid-Based Bio-Nanohybrids for Functional Stabilisation of Influenza Vaccines. *Eur. J. Inorg. Chem.* **2012**, *32*, 5186.
56. Muguruma, H.; Hoshino, T.; Nowaki, K. Electronically type-sorted carbon nanotube-based electrochemical biosensors with glucose oxidase and dehydrogenase", *ACS Appl. Mater. Interfaces* **2015**, *7*, 584.
57. Darder, M.; Takada, K.; Pariente, F.; Lorenzo, E.; Abruna, H. Dithiobissuccinimidyl propionate as an anchor for assembling peroxidases at electrodes surfaces and its application in a H_2O_2 biosensor. *Anal. Chem.* **1999**, *71,* 5530.
58. Yokogama K., Kayanuma Y., CV simulation for electrochemically mediated enzyme reaction and determination of enzyme kinetic constants. *Anal. Chem.* **1998**, *70*, 3368.
59. Darder, M.; Aranda, P.; Hernández-Vélez, M.; Manova E.; Ruiz-Hitzky E. Encapsulation of enzymes in alumina membranes of controlled pore size. *Thin Solid Films* **2006**, *495*, 321.
60. Choi, H. N.; Kim, M. A.; Lee, W.Y. Amperometric glucose biosensor based on sol–gel derived metal oxide/nafion composite films. *Anal. Chem. Acta* **2005**, *537*, 179.
61. Wan, D.; Yuan, S.; Li, G. L.; Neoh K. G.; Kang, E. T. Glucose biosensor from covalent immobilization of chitosan-coupled carbon nanotubes on polyaniline-modified gold electrode. *ACS Appl. Mater. Interfaces* **2010**, *2*, 3083.
62. Zhu, N.; Han, S.; Gan, S.; Ulstrup, J.; Chi, Q. Graphene paper doped with chemically compatible prussian blue nanoparticles as nanohybrid electrocatalyst. *Adv. Funct. Mater.* **2013**, *23*, 5297.
63. Papa, H.; Gaillard, M.; Gonzalez, L.; Chatterjee, J. Fabrication of functionalized carbon nanotube buckypaper electrodes for application in glucose biosensors. *Biosensors* **2014**, *4*, 449.
64. Marand, Z. R.; Shahtahmassebi, N.; Housaindokht, M. R.; Rounaghi G. H.; Razavipanah, I. Construction of an amperometric glucose biosensor by immobilization of glucose oxidase on nanocomposite at the surface of FTO electrode. *Electroanalysis* **2014**, *26*, 840.

65. Ji, J.; Joh, H-I.; Chunga Y.; Kwon, Y. Glucose oxidase and polyacrylic acid based water swellable enzyme–polymer conjugates for promoting glucose detection. *Nanoscale* **2017**, *9*, 15998.
66. Logan, B.; Hamelers, B.; Rozendal, R.; Schoder, U.; Keller, J.; Freguia, S.; Aelterman, P.; Verstraete W.; Elrabaey, K. Microbial fuel cells: Methodology and technology. *Environ. Sci. Technol*. **2006**, *40*, 5181.
67. Falk, M.; Blum, Z.; Shleev, S. Direct electron transfer based enzymatic fuel cells. *Electrochim. Acta* **2012**, *82*, 191.
68. Campbell, A. S.; Jeong, Y. J.; Geier, S. M.; Koepsel, R. R.; Russell, A. J.; Islam, M. F. Membrane/mediator-free rechargeable enzymatic biofuel cell utilizing graphene/single-wall carbon nanotube cogel electrodes. *ACS Appl. Mater. Interfaces* **2015**, *7*, 4056.
69. Liu, Y.; Zhang, J.; Cheng, Y., Jiang, S. P. Effect of carbon nanotubes on direct electron transfer and electrocatalytic activity of immobilized glucose oxidase. *ACS Omega* **2018**, *3*, 667.
70. Cinquin, P.; Gondran, C.; Giroud, F.; Mazabrard, S.; Pellissier, A.; Boucher, F.; Alcaraz, J. P.; Gorgy, K.; Lenouvel, F.; Mathe, S.; Porcu, P.; Cosnier, S. A glucose biofuel cell implanted in rats. *PLoS ONE* **2010**, *5*, 1.
71. Zebda, A.; Cosnier, S.; Alcaraz, J. P.; Holzinger, M.; Le Goff, A.; Gondran, C.; Boucher, F.; Giroud, F.; Gorgy, K.; Lamraoui, H.; Cinquin, P. Single glucose biofuel cells implanted in rats power electronic devices. *Sci. Rep.* **2013**, *3*, 1516.
72. Trifonov, A.; Herkendell, K.; Tel-Vered, R.; Yehezkeli, O.; Woerner, M.; Willner, I. Enzyme-capped relay-functionalized mesoporous carbon nanoparticles: effective bioelectrocatalytic matrices for sensing and biofuel cell applications. *ACS Nano* **2013**, *7*, 11358.
73. Min, K.; Heon Ryu, J.; Je Yoo, Y. Mediator-free glucose/O_2 biofuel cell based on a 3-dimensional glucose oxidase/SWNT/polypyrrole composite electrode. *Biotechnol. Bioproc. E.* **2010**, *15*, 371.
74. Falk, M.; Andoralov, V.; Blum, Z.; Sotres, J.; Suyatin, DB.; Ruzgas, T.; Arnebrant, T.; Shleev. Biofuel cell as a power source for electronic contact lenses. *Biosens. Bioelectron.* **2012**, *37*, 38.
75. Garcia-Perez, T.; Hong, S. G.; Kim, J.; Ha, S. Entrapping cross-linked glucose oxidase aggregates within a graphitized mesoporous carbon network for enzymatic biofuel cells. *Enzym. Microb. Technol*. **2016**, *90*, 26.

76. Reid, R. C.; Jones, S. R.; Hickey, D. P.; Minteer, S. D.; Gale, B. K. Modeling carbon nanotube connectivity and surface activity in a contact lens biofuel cell. *Electrochim. Acta* **2016**, *203*, 30.